Stimulated scintillation emission depletion X-ray imaging

Alekhin, Mikhail S ; Patton, Gaël ; Dujardin, Christophe ; Douissard, Paul A ; Lebugle, Maxime ; Novotny, Lukas ; Stampanoni, Marco

DOI: https://doi.org/10.1364/oe.25.000654

Research Article | Vol. 25, No. 2 | 23 Jan 2017 | OPTICS EXPRESS 654

Optics EXPRESS

Stimulated scintillation emission depletion X-ray imaging

M. S. ALEKHIN,[1,2,*] G. PATTON,[3,4] C. DUJARDIN,[3] P. -A. DOUISSARD,[5] M. LEBUGLE,[2] L. NOVOTNY,[6] AND M. STAMPANONI[1,2]

[1]*Institute for Biomedical Engineering, ETH Zürich, Zürich, Switzerland*
[2]*Swiss Light Source, Paul Scherrer Institut, Villigen, Switzerland*
[3]*Université Claude Bernard Lyon1, CNRS, Institut Lumière Matière, F-69622 Villeurbanne, France*
[4]*Icohup S.A.S, Limoges, France*
[5]*European Synchrotron Radiation Facility, Grenoble, France*
[6]*Photonics Laboratory, ETH Zürich, Zürich, Switzerland*
[*]*mikhail.alekhin@alumni.ethz.ch*

Abstract: X-ray microtomography is a widely applied tool for noninvasive structure investigations. The related detectors are usually based on a scintillator screen for the fast in situ conversion of an X-ray image into an optical image. Spatial resolution of the latter is fundamentally diffraction limited. In this work, we introduce stimulated scintillation emission depletion (SSED) X-ray imaging where, similar to stimulated emission depletion (STED) microscopy, a depletion beam is applied to the scintillator screen to overcome the diffraction limit. The requirements for the X-ray source, the X-ray flux, the scintillator screen, and the STED beam were evaluated. Fundamental spatial resolution limits due to the spread of absorbed X-ray energy were estimated with Monte Carlo simulations. The SSED proof-of-concept experiments demonstrated 1) depletion of X-ray excited scintillation, 2) partial confinement of scintillating regions to sub-diffraction sized volumes, and 3) improvement of the imaging contrast by applying SSED.

OCIS codes: (110.7440) X-ray imaging; (100.6640) Superresolution; (290.5930) Scintillation; (160.5690) Rare-earth-doped materials; (000.2170) Equipment and techniques; (310.6845) Thin film devices and applications.

References and links

1. B. P. Flannery, H. W. Deckman, W. G. Roberge, and K. L. D'Amico, "Three-dimensional X-ray microtomography," Science **237**(4821), 1439–1444 (1987).
2. A. Koch, C. Raven, P. Spanne, and A. Snigirev, "X-ray imaging with submicrometer resolution employing transparent luminescent screens," J. Opt. Soc. Am. A **15**(7), 1940–1951 (1998).
3. M. Born and E. Wolf, *Principles of Optics: Electromagnetic Theory of Propagation, Interference and Diffraction of Light* (Cambridge University Press, 1999).
4. A. Sakdinawat and D. Attwood, "Nanoscale X-ray imaging," Nat. Photonics **4**(12), 840–848 (2010).
5. S. W. Hell and J. Wichmann, "Breaking the diffraction resolution limit by stimulated emission: stimulated-emission-depletion fluorescence microscopy," Opt. Lett. **19**(11), 780–782 (1994).
6. S. W. Hell, "Far-field optical nanoscopy," Science **316**(5828), 1153–1158 (2007).
7. S. W. Hell, "Toward fluorescence nanoscopy," Nat. Biotechnol. **21**(11), 1347–1355 (2003).
8. S. Berning, K. I. Willig, H. Steffens, P. Dibaj, and S. W. Hell, "Nanoscopy in a living mouse brain," Science **335**(6068), 551 (2012).
9. K. I. Willig, B. Harke, R. Medda, and S. W. Hell, "STED microscopy with continuous wave beams," Nat. Methods **4**(11), 915–918 (2007).
10. G. Vicidomini, G. Moneron, K. Y. Han, V. Westphal, H. Ta, M. Reuss, J. Engelhardt, C. Eggeling, and S. W. Hell, "Sharper low-power STED nanoscopy by time gating," Nat. Methods **8**(7), 571–573 (2011).
11. D. S. Hamilton, S. K. Gayen, G. J. Pogatshnik, R. D. Ghen, and W. J. Miniscalco, "Optical-absorption and photoionization measurements from the excited states of Ce3+:Y3Al5O12," Phys. Rev. B Condens. Matter **39**(13), 8807–8815 (1989).
12. L. Schermelleh, R. Heintzmann, and H. Leonhardt, "A guide to super-resolution fluorescence microscopy," J. Cell Biol. **190**(2), 165–175 (2010).
13. T. Martin and A. Koch, "Recent developments in X-ray imaging with micrometer spatial resolution," J. Synchrotron Radiat. **13**(2), 180–194 (2006).
14. M. Nikl and A. Yoshikawa, "Recent R&D trends in inorganic single-crystal scintillator materials for radiation detection," Adv. Opt. Mater. **3**(4), 463–481 (2015).

#281472 http://dx.doi.org/10.1364/OE.25.000654
Journal © 2017 Received 25 Nov 2016; revised 21 Dec 2016; accepted 26 Dec 2016; published 9 Jan 2017

Optics EXPRESS

15. scintillator.lbl.gov.
16. P.-A. Douissard, A. Cecilia, T. Martin, V. Chevalier, M. Couchaud, T. Baumbach, K. Dupré, M. Kühbacher, and A. Rack, "A novel epitaxially grown LSO-based thin-film scintillator for micro-imaging using hard synchrotron radiation," J. Synchrotron Radiat. **17**(5), 571–583 (2010).
17. Y. Zorenko, M. Nikl, V. Gorbenko, V. Savchyn, T. Voznyak, R. Kucerkova, O. Sidletskiy, B. Grynyov, and A. Fedorov, "Growth and luminescent properties of Lu2SiO5 and Lu2SiO5:Ce single crystalline films," Opt. Mater. **33**(6), 846–852 (2011).
18. G. Hajdok, J. J. Battista, and I. A. Cunningham, "Fundamental x-ray interaction limits in diagnostic imaging detectors: spatial resolution," Med. Phys. **35**(7), 3180–3193 (2008).
19. G. Bizarri, W. W. Moses, J. Singh, A. N. Vasil'ev, and R. T. Williams, "An analytical model of nonproportional scintillator light yield in terms of recombination rates," J. Appl. Phys. **105**(4), 044507 (2009).
20. B. L. Henke, E. M. Gullikson, and J. C. Davis, "X-ray interactions: photoabsorption, scattering, transmission, and reflection at E = 50-30,000 eV, Z = 1-92," Atom. Data Nucl. Data **54**(2), 181–342 (1993).
21. G. F. Knoll, *Radiation Detection and Measurement*, 3rd ed. (John Wiley and Sons, Inc., 2000).
22. S. Agostinelli, J. Allison, K. Amako, J. Apostolakis, H. Araujo, P. Arce, M. Asai, D. Axen, S. Banerjee, G. Barrand, F. Behner, L. Bellagamba, J. Boudreau, L. Broglia, A. Brunengo, H. Burkhardt, S. Chauvie, J. Chuma, R. Chytracek, G. Cooperman, G. Cosmo, P. Degtyarenko, A. Dell'Acqua, G. Depaola, D. Dietrich, R. Enami, A. Feliciello, C. Ferguson, H. Fesefeldt, G. Folger, F. Foppiano, A. Forti, S. Garelli, S. Giani, R. Giannitrapani, D. Gibin, J. J. Gómez Cadenas, I. González, G. Gracia Abril, G. Greeniaus, W. Greiner, V. Grichine, A. Grossheim, S. Guatelli, P. Gumplinger, R. Hamatsu, K. Hashimoto, H. Hasui, A. Heikkinen, A. Howard, V. Ivanchenko, A. Johnson, F. W. Jones, J. Kallenbach, N. Kanaya, M. Kawabata, Y. Kawabata, M. Kawaguti, S. Kelner, P. Kent, A. Kimura, T. Kodama, R. Kokoulin, M. Kossov, H. Kurashige, E. Lamanna, T. Lampén, V. Lara, V. Lefebure, F. Lei, M. Liendl, W. Lockman, F. Longo, S. Magni, M. Maire, E. Medernach, K. Minamimoto, P. Mora de Freitas, Y. Morita, K. Murakami, M. Nagamatu, R. Nartallo, P. Nieminen, T. Nishimura, K. Ohtsubo, M. Okamura, S. O'Neale, Y. Oohata, K. Paech, J. Perl, A. Pfeiffer, M. G. Pia, F. Ranjard, A. Rybin, S. Sadilov, E. Di Salvo, G. Santin, T. Sasaki, N. Savvas, Y. Sawada, S. Scherer, S. Sei, V. Sirotenko, D. Smith, N. Starkov, H. Stoecker, J. Sulkimo, M. Takahata, S. Tanaka, E. Tcherniaev, E. Safai Tehrani, M. Tropeano, P. Truscott, H. Uno, L. Urban, P. Urban, M. Verderi, A. Walkden, W. Wander, H. Weber, J. P. Wellisch, T. Wenaus, D. C. Williams, D. Wright, T. Yamada, H. Yoshida, and D. Zschiesche, "GEANT4 - a simulation toolkit," Nucl. Instrum. Methods Phys. Res. A **506**(3), 250–303 (2003).
23. V. Vistovskyy, Y. Chornodolskyy, A. Gloskovskii, S. Syrotyuk, T. Malyi, M. Chylii, P. Zhmurin, A. Gektin, A. Vasil'ev, and A. Voloshinovskii, "Modeling of X-ray excited luminescence intensity dependence on the nanoparticle size," Radiat. Meas. **90**, 174–177 (2016).
24. A. Belsky, K. Ivanovskikh, A. Vasil'ev, M.-F. Joubert, and C. Dujardin, "Estimation of the electron thermalization length in ionic materials," J. Phys. Chem. Lett. **4**(20), 3534–3538 (2013).
25. Z. Wang, Y. Xie, B. D. Cannon, L. W. Campbell, F. Gao, and S. Kerisit, "Computer simulation of electron thermalization in CsI and CsI(Tl)," J. Appl. Phys. **110**(6), 064903 (2011).
26. W. W. Moses, G. A. Bizarri, R. T. Williams, S. A. Payne, A. N. Vasil'ev, J. Singh, Q. Li, J. Q. Grim, and W. Choong, "The origins of scintillator non-proportionality," IEEE Trans. Nucl. Sci. **59**(5), 2038–2044 (2012).
27. R. T. Williams, J. Q. Grim, Q. Li, K. B. Ucer, and W. W. Moses, "Excitation density, diffusion-drift, and proportionality in scintillators," Phys. Status Solidi, B Basic Res. **248**(2), 426–438 (2011).
28. J. Q. Grim, Q. Li, K. B. Ucer, A. Burger, G. A. Bizarri, W. W. Moses, and R. T. Williams, "The roles of thermalized and hot carrier diffusion in determining light yield and proportionality of scintillators," Phys. Status Solidi., A Appl. Mater. Sci. **209**(12), 2421–2426 (2012).
29. R. Kirkin, V. V. Mikhailin, and A. N. Vasil'ev, "Recombination of correlated electron-hole pairs with account of hot capture with emission of optical phonons," IEEE Trans. Nucl. Sci. **59**(5), 2057–2064 (2012).
30. F. Gao, Y. L. Xie, Z. G. Wang, S. Kerisit, D. X. Wu, L. W. Campbell, R. M. Van Ginhoven, and M. Prange, "Monte Carlo simulation of gamma-ray response of BaF2 and CaF2," J. Appl. Phys. **114**(17), 173512 (2013).
31. M. Stampanoni, G. Borchert, P. Wyss, R. Abela, B. Patterson, S. Hunt, D. Vermeulen, and P. Rüegsegger, "High resolution X-ray detector for synchrotron-based microtomography," Nucl. Instrum. Methods Phys. Res. A **491**(1-2), 291–301 (2002).
32. C. G. Bischak, C. L. Hetherington, Z. Wang, J. T. Precht, D. M. Kaz, D. G. Schlom, and N. S. Ginsberg, "Cathodoluminescence-activated nanoimaging: noninvasive near-field optical microscopy in an electron microscope," Nano Lett. **15**(5), 3383–3390 (2015).
33. V. Westphal and S. W. Hell, "Nanoscale resolution in the focal plane of an optical microscope," Phys. Rev. Lett. **94**(14), 143903 (2005).
34. M. S. Alekhin, J. Renger, M. Kasperczyk, P.-A. Douissard, T. Martin, Y. Zorenko, D. A. Vasil'ev, M. Stiefel, L. Novotny, and M. Stampanoni, "STED properties of Ce3+, Tb3+, and Eu3+ doped inorganic scintillators," Opt. Express (2016).
35. A.-L. Bulin, A. Vasil'ev, A. Belsky, D. Amans, G. Ledoux, and C. Dujardin, "Modelling energy deposition in nanoscintillators to predict the efficiency of the X-ray-induced photodynamic effect," Nanoscale **7**(13), 5744–5751 (2015).
36. I. V. Khodyuk, J. T. M. de Haas, and P. Dorenbos, "Nonproportional response between 0.1-100 keV energy by means of highly monochromatic synchrotron X-rays," IEEE Trans. Nucl. Sci. **57**(3), 1175–1181 (2010).

Optics EXPRESS

37. T. Martin, P. A. Douissard, M. Couchaud, A. Cecilia, T. Baumbach, K. Dupre, and A. Rack, "LSO-based single crystal film scintillator for synchrotron-based hard X-ray micro-imaging," IEEE Trans. Nucl. Sci. **56**(3), 1412–1418 (2009).
38. G. E. Jellison, Jr., E. D. Specht, L. A. Boatner, D. J. Singh, and C. L. Melcher, "Spectroscopic refractive indices of monoclinic single crystal and ceramic lutetium oxyorthosilicate from 200 to 850 nm," J. Appl. Phys. **112**(6), 063524 (2012).
39. M. Stampanoni, A. Groso, A. Isenegger, G. Mikuljan, Q. Chen, D. Meister, M. Lange, R. Betemps, S. Henein, and R. Abela, "TOMCAT: a beamline for TOmographic Microscopy and Coherent rAdiology experimenTs," AIP Conf. Proc. **879**, 848–851 (2007).
40. G. Lovric, R. Mokso, C. M. Schlepütz, and M. Stampanoni, "A multi-purpose imaging endstation for high-resolution micrometer-scaled sub-second tomography," Phys. Med. **32**(12), 1771–1778 (2016).
41. R. K. Singh, P. Senthilkumaran, and K. Singh, "Influence of astigmatism and defocusing on the focusing of a singular beam," Opt. Commun. **270**(2), 128–138 (2007).
42. S. Deng, L. Liu, Y. Cheng, R. Li, and Z. Xu, "Effects of primary aberrations on the fluorescence depletion patterns of STED microscopy," Opt. Express **18**(2), 1657–1666 (2010).
43. X. Hao, C. Kuang, T. Wang, and X. Liu, "Effects of polarization on the de-excitation dark focal spot in STED microscopy," J. Opt. **12**(11), 115707 (2010).
44. A. Cecilia, V. Jary, M. Nikl, E. Mihokova, D. Hänschke, E. Hamann, P. A. Douissard, A. Rack, T. Martin, B. Krause, D. Grigorievc, T. Baumbach, and M. Fiederle, "Investigation of the luminescence, crystallographic and spatial resolution properties of LSO:Tb scintillating layers used for X-ray imaging applications," Radiat. Meas. **62**, 28–34 (2014).
45. D. L. Wood and K. Nassau, "Optical properties of gadolinium gallium garnet," Appl. Opt. **29**(25), 3704–3707 (1990).
46. Y. Kuwano, K. Suda, N. Ishizawa, and T. Yamada, "Crystal growth and properties of (Lu,Y)3Al5O12," J. Cryst. Growth **260**(1-2), 159–165 (2004).
47. A. Cecilia, A. Rack, D. Pelliccia, P. A. Douissard, T. Martin, M. Couchaud, K. Dupré, and T. Baumbach, "Studies of LSO:Tb radio-luminescence properties using white beam hard X-ray synchrotron irradiation," Radiat. Eff. Defects Solids **164**(9), 517–522 (2009).
48. R. H. Webb, "Confocal optical microscopy," Rep. Prog. Phys. **59**(3), 427–471 (1996).
49. V. N. Mahajan, "Aberrated point-spread functions for rotationally symmetric aberrations," Appl. Opt. **22**(19), 3035–3041 (1983).
50. M. J. Nasse and J. C. Woehl, "Realistic modeling of the illumination point spread function in confocal scanning optical microscopy," J. Opt. Soc. Am. A **27**(2), 295–302 (2010).
51. A. Chmyrov, J. Keller, T. Grotjohann, M. Ratz, E. d'Este, S. Jakobs, C. Eggeling, and S. W. Hell, "Nanoscopy with more than 100,000 'doughnuts'," Nat. Methods **10**(8), 737–740 (2013).
52. S. Gorelick, V. A. Guzenko, J. Vila-Comamala, and C. David, "Direct e-beam writing of dense and high aspect ratio nanostructures in thick layers of PMMA for electroplating," Nanotechnology **21**(29), 295303 (2010).
53. J. Vila-Comamala, S. Gorelick, E. Färm, C. M. Kewish, A. Diaz, R. Barrett, V. A. Guzenko, M. Ritala, and C. David, "Ultra-high resolution zone-doubled diffractive X-ray optics for the multi-keV regime," Opt. Express **19**(1), 175–184 (2011).
54. H. Mimura, S. Handa, T. Kimura, H. Yumoto, D. Yamakawa, H. Yokoyama, S. Matsuyama, K. Inagaki, K. Yamamura, Y. Sano, K. Tamasaku, Y. Nishino, M. Yabashi, T. Ishikawa, and K. Yamauchi, "Breaking the 10 nm barrier in hard-X-ray focusing," Nat. Phys. **6**(2), 122–125 (2009).
55. A. Snigirev, V. Kohn, I. Snigireva, and B. Lengeler, "A compound refractive lens for focusing high-energy X-rays," Nature **384**(6604), 49–51 (1996).
56. C. G. Schroer, O. Kurapova, J. Patommel, P. Boye, J. Feldkamp, B. Lengeler, M. Burghammer, C. Riekel, L. Vincze, A. van der Hart, and M. Küchler, "Hard x-ray nanoprobe based on refractive x-ray lenses," Appl. Phys. Lett. **87**(12), 124103 (2005).
57. A. J. Morgan, M. Prasciolu, A. Andrejczuk, J. Krzywinski, A. Meents, D. Pennicard, H. Graafsma, A. Barty, R. J. Bean, M. Barthelmess, D. Oberthuer, O. Yefanov, A. Aquila, H. N. Chapman, and S. Bajt, "High numerical aperture multilayer Laue lenses," Sci. Rep. **5**, 9892 (2015).
58. H. Yan, V. Rose, D. Shu, E. Lima, H. C. Kang, R. Conley, C. Liu, N. Jahedi, A. T. Macrander, G. B. Stephenson, M. Holt, Y. S. Chu, M. Lu, and J. Maser, "Two dimensional hard x-ray nanofocusing with crossed multilayer Laue lenses," Opt. Express **19**(16), 15069–15076 (2011).
59. I. A. Shcherbakov, A. I. Zagumennyi, and V. A. Mikhailov, "Rare earth ion lasers Nd3+," in *Handbook of Laser Technology and Applications* (Taylor & Francis, 2003), pp. 353–382.
60. R. Wu, Q. Zhan, H. Liu, X. Wen, B. Wang, and S. He, "Optical depletion mechanism of upconverting luminescence and its potential for multi-photon STED-like microscopy," Opt. Express **23**(25), 32401–32412 (2015).

1. Introduction

X-ray microtomography is a powerful technique for investigating the internal structure of opaque objects [1]. An X-ray beam penetrates a sample, and the spatial distribution of the X-ray attenuation coefficient is read out by a detector. The detector is usually based on a

Optics EXPRESS

scintillator screen that converts X-rays into optical photons. The optical image generated in the scintillator screen is magnified with a microscope objective and recorded by a photodetector. Even though X-ray wavelengths theoretically allow imaging with sub-nanometer spatial resolution, in practice the finite X-ray energy deposition volume and the diffraction barrier of the microscope optics limit the achievable resolution [2]. The diffraction limit is given by $\approx\lambda/2NA$, where λ is the wavelength of the scintillation emission, and NA is the numerical aperture of the objective [3]. It is 300-500 nm for current imaging systems. Use of X-ray optics is a well-established solution for sub-100-nm X-ray imaging [4], but it requires fabrication of additional tools, and in some cases a monochromatic and coherent X-ray beam.

In far-field fluorescence microscopy, the diffraction limit was overcome with stimulated emission depletion (STED), which improved the spatial resolution down to the nanometer scale [5, 6]. This technique employs a STED-laser beam that instantly de-excites fluorescent markers from the excited state to the ground state via stimulated emission. Usually, the STED beam has a doughnut shape that confines the fluorescence region to its very center. The image is then formed by raster scanning the doughnut along the specimen and measuring the fluorescence from its zero-intensity region. The size of the zero-intensity region determines the imaging resolution.

In this work, we introduce the concept for stimulated scintillation emission depletion (SSED) X-ray imaging. It combines STED nanoscopy with conventional scintillator-based X-ray imaging to improve the spatial resolution of the latter. This technique requires neither coherent or monochromatic X-rays, nor X-ray optics. First, we describe the concept and evaluate the requirements for the X-ray source, the STED laser, and the scintillator. Next, we perform Monte Carlo (MC) simulations to estimate the fundamental resolution limits due to finite volume X-ray energy deposition. Finally, we demonstrate experimentally that X-ray excited scintillation can be depleted by a STED-laser, the scintillating region can thereby be spatially confined, and X-ray imaging contrast can be improved by applying SSED.

2. SSED X-ray imaging concept

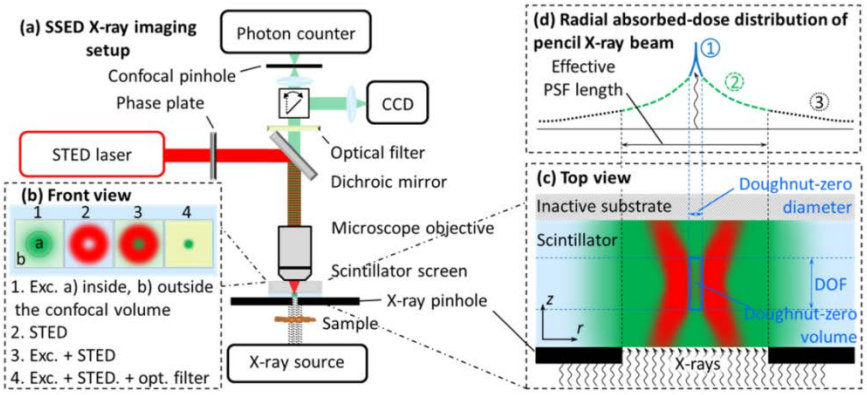

Fig. 1. (a) Top view of the proposed setup for SSED X-ray imaging. (b) Front view of the scintillator screen through the confocal pinhole. (c) Top view of the scintillator screen. (d) Schematic of radial absorbed-dose distribution of a pencil X-ray beam incident on the doughnut center, where 1 shows the contribution to the scintillation from the doughnut-zero volume, 1 + 2 shows the contribution to the visibility and the spatial resolution, 3 shows the remaining tails not affecting SSED X-ray imaging.

The setup for SSED X-ray imaging is schematically shown in Fig. 1. An X-ray source produces an X-ray beam that penetrates through a sample. A scintillator screen absorbs the beam and converts its spatial intensity distribution into a spatial distribution of the excited luminescence centers. A STED laser generates a STED beam [6, 7] directed with a dichroic

Optics EXPRESS

mirror toward a microscope objective, whereby it is focused on the scintillator. An optical element(s), e. g. a phase plate, alters the STED beam creating at least one zero-intensity point, e. g. a doughnut, at a defined position in the objective focal plane, see Fig. 1(b). The STED light instantly de-excites the X-ray excited luminescence centers except those located within narrow-sized volumes around the zero-intensity points of the STED laser, which we will refer to as doughnut-zero volumes. The scintillation emitted from these volumes is collected by the same objective and recorded by a photo-detector. An optical filter is placed in front of the detector to block the STED light. The image of the object in the scintillator screen is scanned relative to the position of the zero-intensity points, and a two-dimensional X-ray image of one projection of the sample is reconstructed. In the case of a single doughnut, a confocal pinhole is placed in front of the photodetector to reduce the detection of out-of-focus scintillation emission. An X-ray pinhole can be placed in front of the scintillator screen, firstly, to reduce the contribution of the finite volume X-ray energy deposition (Section 3.2), and secondly, to minimize the detection of scintillation emitted from out-of-focus regions (Section 4.2).

STED-nanoscopy has been successfully implemented in both pulsed [8] and continuous-wave (cw) [9, 10] modes. For SSED X-ray imaging, we use continuous X-ray excitation, cw-STED laser depletion, and simultaneous scintillation detection. We expect several advantages over the pulsed SSED which employs consecutive excitation, depletion, and scintillation detection. First, no synchronization of the X-ray pulses with the STED-laser pulses is required. Second, the STED laser can cause excited state absorption (ESA) of the excited electrons into higher energy bands [11], which competes with the stimulated emission process. The ESA electrons might return to the same excited states and relax via spontaneous emission. In the case of the pulsed techniques, this emission might occur within the detection time-window. In the case of the cw-STED, it is continuously depleted. Finally, peak power of a pulsed STED laser is always higher than its time-averaged power. This increases the probability of undesired multi-photon excitation by the STED laser.

3. SSED X-ray imaging requirements

3.1 Scintillator requirements

In SSED X-ray imaging, the doughnut-zero volume from which the scintillation emission is detected can be roughly approximated by an ellipsoid sized 30-100 nm perpendicular to the optical axis, and 1-1.5 μm along the optical axis, considering the detection from a >1.8 refractive index scintillator using a high-NA air immersion objective [12]. High X-ray absorption and conversion efficiencies are therefore crucial scintillator requirements for SSED X-ray imaging. They imply high density, high effective atomic number Z_{eff}, and high light yield of the scintillation material (the number of emitted optical photons per absorbed radiation energy). From a list of scintillators with optimal properties [13–15], we select Lu_2SiO_5 (LSO) doped with Ce or Tb and use them in the following calculations. To minimize the signal from out-of-focus planes, the thickness of the scintillator should be comparable to the DOF of the objective, see Fig. 1(c). To achieve this, a single-crystalline scintillator film grown on a non-luminescent substrate can be a suitable option [16, 17].

Finite volume X-ray energy deposition is the next fundamental limit beyond the diffraction barrier. X-rays with energies lower than 100 keV interact with high-Z materials, like LSO, mainly via the photoelectric effect. Fluorescent X-rays and Auger electrons, the products of this interaction, are emitted isotropically. The photoelectrons tend to be emitted perpendicular to the direction of the incident X-rays [18]. The ejected electrons are the main source of finite volume energy deposition on sub-μm range, whereas energy deposition of the characteristic X-rays spreads over much larger volumes. For example, the mean free path of 1-20 keV electrons between interactions in a conventional scintillator is 2-20 nm [19], whereas the attenuation length of 1-20 keV X-rays is 0.3-100 μm [20]. According to the Bethe-Bloch equation, the electron stopping power increases with electron density of the material [21]. This again emphasizes the requirement of high scintillator density.

Optics EXPRESS

3.2 Monte Carlo simulations of X-ray absorbed-dose distributions

Spatial distribution of the X-ray energy deposited in the scintillator was estimated by Monte Carlo simulations based on the GEANT4 toolkit (version 4.9.6 patch 02) and combined with the Livermore package. This extension is applicable for electrons and photons with energies down to 250 eV [22]. In the simulation geometry, similar to those in Refs [2, 18], a monochromatic pencil-like X-ray beam was normally incident on a 170 μm thick and 5 mm radius LSO scintillator disk, a common size of a conventional scintillator screen. The energy deposition was calculated inside a 3 μm thick surface layer oriented toward the X-ray source. The contribution from the backscattered electrons and X-rays from the 167 μm substrate was thereby also included. The layer was divided into concentric hollow cylinders with a 42 nm sampling distance (the difference between the cylinder's inner and outer radii). Additional simulations with a finer sampling distance of 1.3 nm were performed for more accurate estimates of the deposited energy distribution within a 1 μm distance from the X-ray beam. The simulations were performed for monoenergetic X-rays between 8 and 100 keV, with $2 \cdot 10^7$ incident photons for each X-ray energy. The obtained distributions were normalized to the volumes of the sampling cylinders to derive the radial distribution of absorbed X-ray dose per unit mass of the scintillation material $d(r)$, shown in Fig. 2. Normalizing the radial distribution to the unit area yields the radial point spread function $PSF(r)$ of the X-ray interaction [18].

The photon- and electron-transport cutoff distance was set to 1 nm, below which the particle energy was locally deposited. A distance of 1 nm corresponds to the mean free path of ≈1 keV electron in LSO [19]. Lower energy electrons continue to undergo electron-electron interactions, depositing 20-40 eV per scattering until they reach ~20 eV energy. This increases the electron path by several nanometers, a fact not included into our simulations. The broadening of the electron track due to thermalization and diffusion of excitation carriers is estimated to be 2-6 nm in oxide scintillators [19, 23]. Note that in other types of scintillation materials, the electron thermalization length can reach >100 nm [24, 25]. Since the electron has to recombine with a hole to generate light, the spread of the light emission area depends on the travel length of the carriers with the lowest mobility, e. g. holes [26–28]. Especially dedicated tools should in principle be used to simulate these processes in each material individually [25, 29, 30].

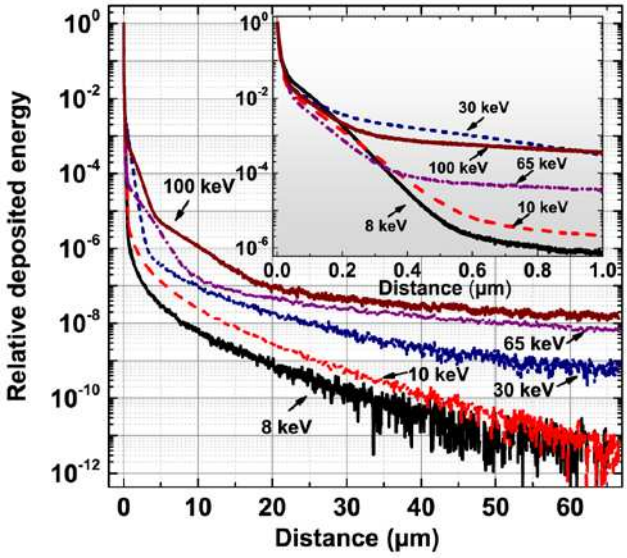

Fig. 2. Monte Carlo simulations of radial X-ray absorbed-dose distributions for various X-ray energies in a 3 μm LSO scintillator layer on a 167 μm LSO substrate.

Optics EXPRESS

Our simulations showed two important features for high-resolution X-ray imaging. The first is a sharp decrease of the radial absorbed-dose distribution, see Fig. 2. A similar decrease was observed in $Y_3Al_5O_{12}$:Ce scintillator by Koch et al. [2]. The full width at half maximum (FWHM) of the radial absorbed-dose distribution in LSO is ≈5 nm for all the simulated X-ray energies. Thermalization paths of <1 keV electrons might further broaden this FWHM by several nanometers, which is still far beyond the diffraction barrier. The second feature is the relatively small total deposited energy in the first scoring volumes around the X-ray beam. For example, the absorbed dose of 10 keV (100 keV) X-rays in a 10 nm radius cylinder is ~10% (~1%) of that absorbed by a 5 mm radius scintillator layer. This might deteriorate the visibility of X-ray imaging with a large field of view (FOV).

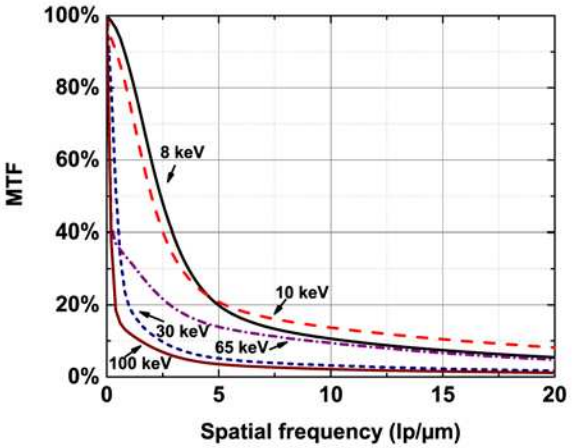

Fig. 3. Monte Carlo simulations of X-ray interaction MTF for a 3 μm LSO scintillator layer on a 167 μm LSO substrate at various X-ray energies. The MTF are derived from X-ray interaction PSF(r) simulated within r ≤ 50 μm from the X-ray beam.

To estimate the visibility deterioration, we calculated the "X-ray interaction" modulation transfer function (MTF) using the Hankel transform of the X-ray interaction PSF [18]

$$MTF\left(k, L/2\right) = H\left\{PSF\left(r\right)\right\} = 2\pi \int_0^{L/2} PSF\left(r\right) J_0\left(2\pi kr\right) rdr \qquad (1)$$

where k is a radial spatial frequency, $L/2$ - is half of the effective PSF length, H is the Hankel transform operator, and J_0 is the zero-order Bessel function. This MTF represents a measurement of the ability to transfer the contrast at a particular spatial-frequency from the X-ray image to the image formed by the X-ray absorbed-dose distribution within the scintillator. $L/2$ is the radial distance from the X-ray beam, within which the X-ray interaction PSF has non-zero values. Regarding the experiment, the effective PSF length represents the central part of the X-ray interaction PSF that contributes to the imaging MTF, see Fig. 1(d). The PSF tails exceeding that length do not contribute and have effectively zero values. Figure 3 compares MTFs at several incident X-ray energies derived from 100 μm long PSFs. MTFs of 8-10 keV X-rays demonstrate good contrast transfer for frequencies up to 5 lp/μm, whereas MTFs of >30 keV X-rays sharply decrease at < 1 lp/μm frequencies. Only a 100 keV X-ray MTF is comparable to those of conventional diffraction limited X-ray imaging systems [31]. Lower X-ray energy responses form substantially better MTFs. Moreover, these MTFs can be further improved by artificial reduction of the PSF length, e. g. by placing smaller-size X-ray pinholes in front of the scintillator screen, as shown in Fig. 1(c).

Optics EXPRESS

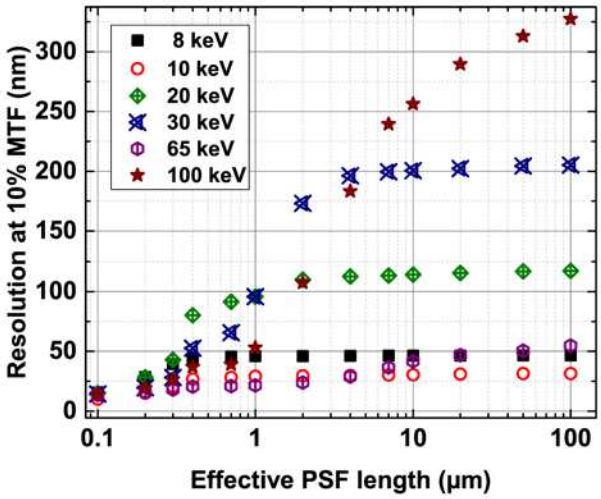

Fig. 4. Simulated spatial resolution expressed in nm at 10% MTF versus the length of X-ray interaction radial point spread function (~X-ray pinhole diameter).

Figure 4 illustrates this effect by comparing spatial resolution at 10% MTF (half of the inverse spatial frequency at 10% MTF) for various X-ray energies and effective X-ray interaction PSF lengths. The use of shorter PSFs improves the resolution. With 0.1 μm long PSFs, the imaging resolution, based on the spread of the absorbed dose, is < 15 nm for all the studied X-ray energies. With 100 μm long PSFs, the resolution worsens to 30 - 300 nm depending on the X-ray energy. The reason for this is the contribution from the PSF's tails. The resolution worsens with increasing incident beam X-ray energy. The exceptions are 10, 13, and 65 keV X-rays, which result in excellent resolution performance for all PSF lengths below 100 μm. Those X-rays interact with LSO mainly via photoelectric effect ejecting 1-4 keV photoelectrons from Lu K-shell (≈63.3 keV binding energy) and L-shells (≈9.2-10.9 keV binding energies), which leave relatively high absorbed doses in the vicinity of the interaction point. Interestingly, scintillator absorbed-dose PSF of a <2.8-keV-electron beam was experimentally observed in recently developed cathodoluminescence-activated imaging method [32]. The effect of the PSF on the resolution was <50 nm despite less dense and smaller Z_{eff} scintillator was used.

3.3 Depletion requirements

SSED X-ray imaging imposes two additional requirements: efficient de-excitation of the excited luminescence centers by the STED-laser and negligible luminescence excited by the STED-laser itself. As in STED nanoscopy, the spatial resolution is approximated by [33]

$$d \approx \frac{\lambda_{STED}}{2NA\sqrt{1+\frac{P_{STED}}{P_s}}} \tag{2}$$

where P_{STED} and λ_{STED} are the power and wavelength of the STED laser, NA is the objective numerical aperture, and P_s is the power of the STED laser at which the probability of the excited luminescence center to be de-excited via stimulated emission is 50%. P_s is given by [9]

$$P_s = \frac{Ahc}{\lambda_{STED}\sigma_{STED}\tau_{fl}} \tag{3}$$

Optics EXPRESS

where h, c, A, σ_{STED}, and τ_{fl} are the Planck constant, the speed of light, the doughnut area, the stimulated emission cross-section and the fluorescence lifetime of the luminescence centers respectively. Efficient de-excitation via stimulated emission depletion therefore requires a tightly focused high power laser beam, as well as a large stimulated emission cross-section and a long fluorescence lifetime of the luminescence centers. Typical scintillator screen luminescence centers are Ce^{3+}, Tb^{3+}, or Eu^{3+} lanthanides [13]. The depletion through 4f-4f transitions of Tb^{3+} and Eu^{3+} require in general lower STED-laser powers compared to 5d-4f transitions of Ce^{3+} [34]. Based on Eq. (2), a resolution improvement to 100-150 nm can be expected with 50…150 mW STED-laser focused in a single doughnut.

3.4 Photodetector signal and X-ray flux requirements

In the following, we estimate the photodetector signal due to the detected scintillation from the doughnut-zero volume; then, we determine the X-ray flux required to excite scintillation of intensity sufficient to surpass possible imaging noise. For this, we introduce the quantum efficiency of SSED X-ray imaging η_{SSED}, defined as the number of photodetector counts per number of the X-rays incident on the scintillator surface below the doughnut-zero volume. We estimate η_{SSED} for 10, 30, 65, and 100 keV X-rays, LSO:Ce and LSO:Tb scintillators, a 0.95NA microscope objective, and a commercially available photodetector. The doughnut-zero volume was approximated by a cylinder with the height equal to the DOF estimated as $n\lambda_{STED}/NA^2 \approx 1.1$ μm, where $n_{LSO} = 1.8$, NA = 0.95, and $\lambda_{STED} \approx 550$ nm. The doughnut-zero diameter was set to 30 and 100 nm corresponding to different values of imaging resolution. The STED beam was focused within the 3 μm thick scintillator surface layer oriented toward the X-ray source. The spatial distribution of the X-ray beam incident on the scintillator surface was uniform.

The quantum efficiency of SSED X-ray imaging was calculated as

$$\eta_{SSED} = \eta_{abs}\eta_{x/v}\eta_{col}\eta_{obj}\eta_{det}\eta_{v/e} \quad (4)$$

η_{abs} is the doughnut-zero absorbed-dose coefficient defined as the X-ray energy deposited within the doughnut-zero volume to total energy of the X-rays incident on the scintillator surface below this volume, see Fig. 1(c). It was calculated as the product of the radial $\eta_{abs\text{-}r}$ and axial $\eta_{abs\text{-}z}$ absorbed-dose coefficients $\eta_{abs} = \eta_{abs\text{-}r}\eta_{abs\text{-}z}$, both derived from the Monte Carlo simulations.

$\eta_{abs\text{-}r}$ is defined as the X-ray energy deposited within the doughnut-zero volume relative to the total X-ray energy deposited within the 5 mm radial extension of this volume, i. e. Ø10 mm x 1.1 μm scintillator layer. The dose absorbed by the doughnut-zero volume was derived using the convolution of the X-ray radial absorbed dose distribution of Fig. 2 with the uniform intensity distribution of the X-rays incident on the doughnut-zero volume. The calculated values of $\eta_{abs\text{-}r}$ are compiled in Table 1. $\eta_{abs\text{-}r}$ is ~2.5-fold higher for Ø100 nm than for Ø30 nm doughnut-zero due to the spread of the absorbed dose of the secondary particles. $\eta_{abs\text{-}r}$ is an order of magnitude higher for 10 keV X-rays than for 100 keV X-rays due to higher relative absorbed-dose of the secondary particles within these scoring regions.

$\eta_{abs\text{-}z}$ is defined as the X-ray energy deposited within the Ø10 mm x 1.1 μm scintillator layer relative to the total energy of the X-rays incident on the scintillator surface below the doughnut-zero volume. The values of $\eta_{abs\text{-}z}$ are compiled in Table 1 as well. $\eta_{abs\text{-}z}$ decreases two orders of magnitude with increasing X-ray energy from 10 to 100 keV. Note that $\eta_{abs\text{-}z}$ are on average 1.5 to 4 times smaller than the tabulated values of the corresponding X-ray absorption efficiencies [20], because MC simulations also take into account the absorbed-dose distribution of the secondary particles within the scintillator and their escape from the scintillator into the outer medium. The latter becomes a crucial aspect when nanoscale scintillators are considered [35].

The conversion efficiency $\eta_{x/v}$ of absorbed X-rays into optical photons is defined as a product of the scintillator light yield and the X-ray energy. The light yield of LSO:Ce is 30-32

Optics EXPRESS

photons per absorbed keV energy (ph/keV) of 662 keV X-rays [14]. However, the absorbed dose by the doughnut-zero volume is mainly due to ~8 keV Auger electrons or 1-2 keV photoelectrons in our particular case of 10, 30, 65, and 100 keV X-rays interacting with LSO:Ce scintillator. Taking into account the non-linearity of the LSO:Ce electron response [36], we estimated its light yield as ≈22 ph/keV. The light yield of LSO:Tb was estimated as $\eta_{x/v}$ ≈28 ph/keV [37]. $\eta_{col} = (NA/2n)^2$ is the objective light collection efficiency. $\eta_{col}^{LSO:Ce}$ = 0.067 and $\eta_{col}^{LSO:Tb}$ = 0.069 for the refractive indexes of 1.81 @ 420 nm and 1.83 @ 550 nm [38]. $\eta_{obj}^{LSO:Ce}$ = 0.065 and $\eta_{obj}^{LSO:Tb}$ = 0.088 is the optical transmittance of the objective. The fraction of the scintillation light that passes through the detection filter that blocks the STED-laser wavelengths is set to η_{det} = 0.8. $\eta_{v/e}^{LSO:Ce}$ = 0.26 and $\eta_{v/e}^{LSO:Tb}$ = 0.48 is the quantum efficiency of the photodetector. η_{obj}, η_{det}, and $\eta_{v/e}$ were corrected for the broad emission spectra of LSO:Ce and LSO:Tb.

The values of η_{SSED} calculated with Eq. (4) are compiled in Table 1. η_{SSED} does not exceed 0.1 photodetector count per one X-ray incident on the scintillator surface below the doughnut-zero volume. The photodetector signal can now be calculated as $P = I_x(\pi d^2/4)\eta_{SSED}$, where d is the doughnut zero cylinder diameter, and I_x is the X-ray flux. The values of P for $I_x = 10^{12}$ ph/mm^2/s are compiled in Table 1. For LSO:Tb, the photodetector signal varies from 800 counts per second (cps) for Ø100 nm doughnut-zero and 10 keV X-rays to ~0.6 cps for Ø30 nm doughnut-zero and 100 keV X-rays. LSO:Ce produces 3.5 lower signal. 100-nm resolution imaging will require then a flux of ~10^9…10^{10} ph/mm^2/s of 10 keV X-rays to overcome moderate photodetector noise of 5 cps. For 30-nm resolution, the flux of ~10^{10}…10^{11} ph/mm^2/s is needed. Therefore, the SSED method is rather suitable for synchrotron X-ray imaging application.

Table 1. Estimation of the photodetector signal due to LSO:Ce and LSO:Tb scintillation from the doughnut-zero volume. Columns from left to right: the X-ray energy; η_{abs-z} - the axial absorbed-dose coefficient; doughnut-zero diameter; η_{abs-r} - the radial absorbed-dose coefficient; η_{SSED} - the quantum efficiency of SSED X-ray imaging; P - the photodetector signal due to $I_x = 10^{12}$ ph/mm^2/s 10 keV X-ray flux.

E_x, keV	η_{abs-z}	Doughnut-zero Ø, nm	η_{abs-r}	LSO:Ce		LSO:Tb	
				η_{SSED}, counts per X-ray	P, cps	η_{SSED}, counts per X-ray	P, cps
10	$6.4\cdot10^{-2}$	100	$2.5\cdot10^{-1}$	$3.1\cdot10^{-2}$	250	$1.0\cdot10^{-1}$	800
		30	10^{-1}	$1.3\cdot10^{-2}$	9	$4.1\cdot10^{-2}$	30
30	$8.8\cdot10^{-3}$	100	$6.3\cdot10^{-2}$	$3.3\cdot10^{-3}$	26	$1.1\cdot10^{-2}$	85
		30	$2.2\cdot10^{-2}$	$1.2\cdot10^{-3}$	0.8	$3.9\cdot10^{-3}$	2.7
65	$1.9\cdot10^{-3}$	100	$9.4\cdot10^{-2}$	$2.4\cdot10^{-3}$	18	$7.7\cdot10^{-3}$	60
		30	$4\cdot10^{-2}$	$9.9\cdot10^{-4}$	0.7	$3.3\cdot10^{-3}$	2.3
100	$9.8\cdot10^{-4}$	100	$3.5\cdot10^{-2}$	$6.8\cdot10^{-4}$	5	$2.2\cdot10^{-3}$	17
		30	$1.3\cdot10^{-2}$	$2.5\cdot10^{-4}$	0.17	$8.1\cdot10^{-4}$	0.57

4. Proof-of-concept experiments

The proof-of-concept experiments were performed at the beamline for Tomographic Microscopy and Coherent Radiology Experiments TOMCAT [39] of the Swiss Light Source with the setup shown in Fig. 1. A nearly-parallel beam (2 mrad x <0.6 mrad divergence) of 12.5 keV X-rays at ~$7\cdot10^{11}$ ph/mm^2/sec flux [40] probed a sample and impinged on a scintillator. The source-to-scintillator distance was 25 m, and the sample-to-scintillator - 20 mm. The scintillator, a 1.6 μm thick single-crystalline film (SCF) of LSO doped with 12% at. Tb^{3+}, was grown on a non-luminescent 170 μm thick Yb_2SiO_5 (YbSO) substrate with a liquid-phase epitaxy (LPE) method by Martin et al [37]. The experiments were performed without an X-ray pinhole, and with Ø 16 μm and Ø 1.8 μm circular X-ray pinholes. The pinholes (cut

Optics EXPRESS

into 25 µm thick W foils by focused ion beam milling using Gallium ions in a FEI Helios dual beam system) were placed 10 mm in front the scintillator resulting in essentially the same diameters of the excited area as the diameters of the pinholes. A STED-laser (cw-628 nm, MPB Communications) was focused with a microscope objective (Nikon Plan Apo 40x/0.95NA air) through the substrate on the scintillator. A vortex phase plate (RPC Photonics, VPP-1a) was used to create a focal doughnut. The polarization direction of the STED-laser was controlled by a half-wave plate (HWP) placed in front of the VPP. A non-polarizing cube beamsplitter was used to direct the STED-laser beam into the microscope objective. The scintillation was collected with the same objective and focused either on a CCD-camera (PCO.2000), or on a single pixel photon counter (Micro Photon Devices, 30 µm, grade F, <3.7 dark cps), which also served as a confocal pinhole. A pair of 544/24 optical filters was used to transmit LSO:Tb emission and block STED-laser photons. The filters were tilted relative to each other to ensure $<10^{-12}$ transmittance at 628 nm. Note that LSO:Tb and 628 nm STED-laser were selected out of a number of other combinations, firstly, because the LSO:Tb excitation can be depleted at relatively low power of the 628 nm laser, and secondly, because of sufficiently weak luminescence of LSO:Tb excited by the 628 nm laser itself [34].

4.1 Doughnut-like PSF

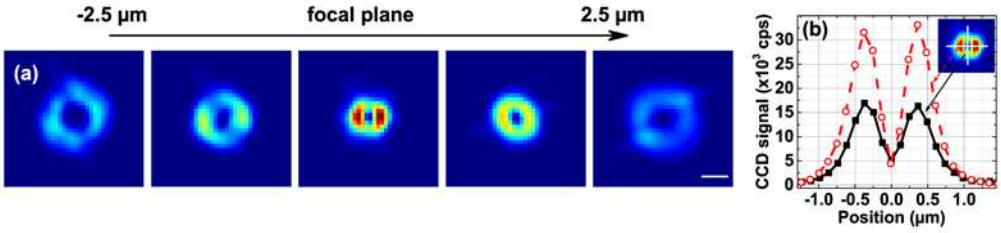

Fig. 5. STED-laser PSF measured as reflection of the STED-laser from the scintillator surface placed at various distances from the objective focal plane. Scale bar is 1 µm. (b) 1D STED-laser PSF intensity profiles measured along the lines in the inset of the figure.

STED-laser PSF functions in Fig. 5 were measured using the reflection of the STED-laser from the scintillator-air surface with the CCD camera as shown in Fig. 1(a). The shape of the PSF was controlled by adjusting a correction collar of the objective and by rotating the STED-laser polarization axis using the HWP. The "doughnut-like" PSF of Fig. 5(a) lacks perfect circular symmetry standard for STED-nanoscopy. Figure 5(b) shows a cross-section through the doughnut, highlighting the low intensity at its center. In fact, due to the finite pixel size of the CCD camera the true intensity at the center is lower than what is measured. Rotation of the polarization axis by 90°, 180°, and 270° resulted in the same PSF-shapes respectively. Other directions of the polarization axis resulted in stronger disturbed PSFs, closely resembling the astigmatism-affected ones [41,42]. Circular polarization, required to obtain zero-intensity in the center of the doughnut [43], resulted in superposition of the "doughnut-like" and the disturbed PSFs, which was avoided. Linear laser polarization with the axis direction resulting in the "doughnut-like" PSF of Fig. 5(a) was used in the following proof-of-concept experiments.

Observed astigmatism could be caused by birefringence of the scintillator substrate. LSO has refractive indexes of $n_{11} \approx n_{22} \approx 1.8$ and $n_{33} \approx 1.82$ at 628 nm [38]. The substrate, YbSO, has the same crystal structure as LSO with slightly different lattice parameters [44]. Higher quality doughnuts can be achieved with scintillator materials having cubic crystal structure, such as $Y_3Al_5O_{12}$, $Lu_3Al_5O_{12}$, or $Gd_3Ga_5O_{12}$ [45, 46].

4.2 Scintillation depletion measurements

In the first proof-of-concept experiment, the X-ray excited scintillation signal of LSO:Tb was measured as a function of STED-laser power using the photon counter, see Fig. 6. The

Optics EXPRESS

measurements were performed without, with the 16 μm, and the 1.8 μm X-ray pinhole. The STED-laser was focused through the substrate into the central region of the excited scintillator area with the doughnut-like PSF of Fig. 5(a).

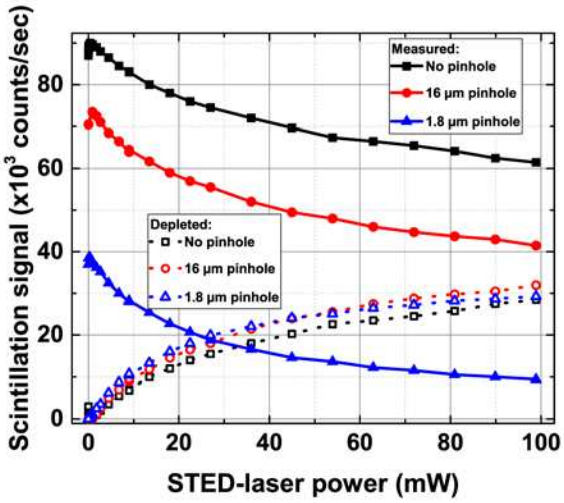

Fig. 6. (Solid curves) X-ray excited scintillation signal of LSO:Tb as a function of 628 nm STED-laser power. (Dotted curves) Depleted scintillation signal, derived as a difference between the original and the signal remaining under the depletion. The STED-laser power was measured before the objective and corrected for the objective transmittance.

The X-ray excited scintillation signal decreases with increasing STED-laser power, similar to the optically excited luminescence [34]. Remarkably, we did not detect any additional excitation due to possible interaction of STED-laser photons with X-ray absorption products, e. g. conduction band electrons. Only a 3-4% increase of the scintillation signal was observed with increasing STED-laser power from 0 to ~1 mW. This signal was ascribed to optically stimulated release of the traps which are filled when LSO:Tb is excited by X-rays [47].

A substantial fraction of the scintillation signal, however, could not be depleted. We will refer to it as "undepletable" scintillation. Its signal is ~60,000 cps using no X-ray pinhole, ~40,000 cps using the 16 μm pinhole, and ~10,000 cps using the 1.8 μm pinhole, corresponding to 67%, 57%, and 25% of the original scintillation signal, respectively. Those fractions are higher than 14% in the case of focused optical laser excitation [34]. The depleted signal, plotted as dotted curves in Fig. 6, is the same in all three cases. Clearly, the size of the excitation pattern affects the amount of the detected "undepletable" scintillation. This background scintillation is either emitted outside the depletion region and then detected due to scattering or reflection events, or this is scintillation directly detected from outer Airy rings of the microscope PSF.

In confocal optical microscopy, both the observation and the illumination PSF are described by Airy diffraction patterns, which are the same when the same optics is used [48]. The resulting imaging PSF is a product of the two, and the signal originating from the Airy rings is negligibly small. In SSED, however, the X-ray illumination pattern is homogeneous, resulting in a higher fraction of the signal detected from the Airy rings. In an ideal confocal detection system, this fraction is 16.2% [3]. We observed as much as 67%. Theoretically, this fraction can be even higher due to spherical aberrations [49] or astigmatism [41]. In our case, the spherical aberrations can originate from refractive index mismatch between the designed for n = 1.515 cover glass microscope objective and the n≈1.8 scintillator substrate. To estimate the effect of aberrations, we employed a "PSF Lab" simulation software, which calculates the illumination PSF of the beam focused through several layers by high-NA

Optics EXPRESS

objectives operated under non-design conditions [50]. The fraction of the emission detected from the Airy rings region can be indeed ≥67% for our experimental conditions. Since the thickness of the scintillator, 1.6 μm, is comparable to the DOF of the detection system, 1.1 μm, most of the signal associated with outer Airy-rings actually originates from the objective focal plane. Therefore, we will refer to it as "out-of-confocal-volume" signal rather than "out-of-focus".

The detected "undepletable" scintillation signal is expected to deteriorate the contrast of SSED X-ray imaging. Independent of the proposed origin, the signal can be minimized by using e. g. an X-ray pinhole allowing X-rays to impinge on the scintillator only within the confocal volume. A better solution could be parallelization of SSED using a wide-field nonlinear structured depletion pattern, which has been successfully implemented with wide-field excitation in super-resolution microscopy [51].

4.3 Spatial confinement of the scintillation signal

Next, we demonstrate the possibility of spatial confinement of the scintillation signal by the STED-laser. The scintillator was excited on an area of Ø 1.8 micrometers and the donut-shaped depletion laser has been focused into the center of this area. The resulting scintillation emission, imaged with the CCD, is shown together with corresponding intensity profiles in Figs. 7(a)-7(e). The inset in Fig. 7(e) shows the fraction of the scintillation remaining under the depletion, calculated by dividing the scintillation profiles at various STED-laser powers over the scintillation profile at 0 mW.

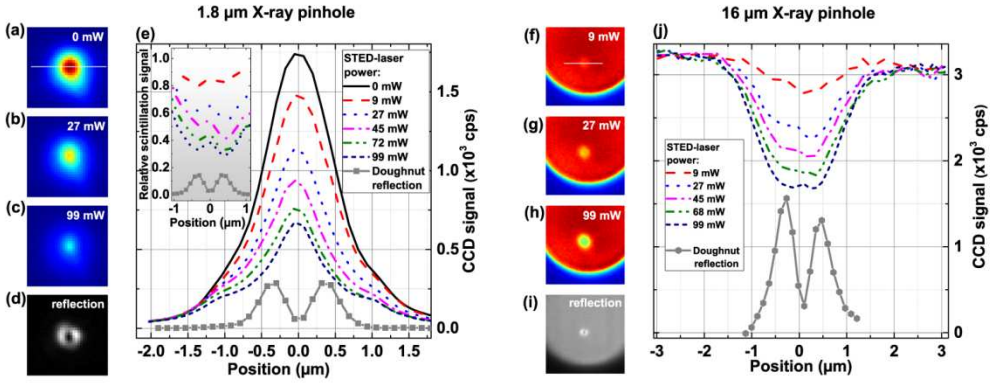

Fig. 7. Scintillation of LSO:Tb excited by X-rays passing through the 1.8 μm (a-e) and the 16 μm (f-k) X-ray pinholes measured with the CCD camera. (a-c) and (f-h) - 2D scintillation intensity maps at various STED-laser powers. (d,i) - reflection of the STED-laser doughnuts measured without the detection filters, in case of (i) - on top of the scintillation. (e,j) - 1D intensity profiles measured along the lines of Figs. (a,f).

The scintillation signal decreases non-uniformly within the crystal. At 99 mW, the intensity drops to ~40% in the center of the doughnut, and to ~30% - at the rim. To the best of our knowledge, this is the first observation of spatial confinement of scintillation using a STED-laser. However, the observed ratio of the signal remaining in the doughnut-center to the signal remaining in the doughnut-rim is currently too low for practical applications. As discussed in Section 4.1, the aberrations-distorted doughnut with non-zero intensity in its center is currently the main limitation. Additionally, as discussed in section 4.2, there is a residual scintillation signal that originates from outside of the confocal volume. This effect can be demonstrated with a larger, Ø 16 μm, excitation area in Figs. 7(f)-7(j), for which the center-to-rim contrast vanishes in the scintillator signal that emerges from outside of the confocal volume.

Optics EXPRESS

4.4 SSED scans

Our final proof-of-concept experiment demonstrates an improvement of the contrast of the X-ray imaging. For this, a 2.1-μm thick 1D Au grating with various linewidths down to 300 nm and 50% duty cycle was grown in polymethyl-methacrylate resist molds prepared by e-beam lithography (Vistec EBPG 5000plus) on a 250-nm thick Si_3N_4 substrate [52]. The electroplated Au has an estimated density of 17 g/cm^3, allowing 56% transmission of the 12.5-keV X-rays. A scanning electron microscope image of the 300 nm lw grating is shown in Fig. 8(a). An X-ray image of the 300 nm lw grating made with the diffraction-limited microscope of Fig. 1 using the CCD camera is shown in Fig. 8(b). In the proof-of-concept experiment, the grating, placed on the "sample" position in Fig. 1, was moved step-wise with a piezo stage (P-612.2 XY, PI) with step-size of 60 nm. After each step, the photon counter registered the scintillation signal during 4 sec. The 1.8 μm X-ray pinhole was used to minimize the detection of out-of-confocal-volume scintillation. The STED-laser was focused to the center of the excited scintillation area as shown in Fig. 7. The scans were repeated multiple times along the same line with the STED laser switched on and off.

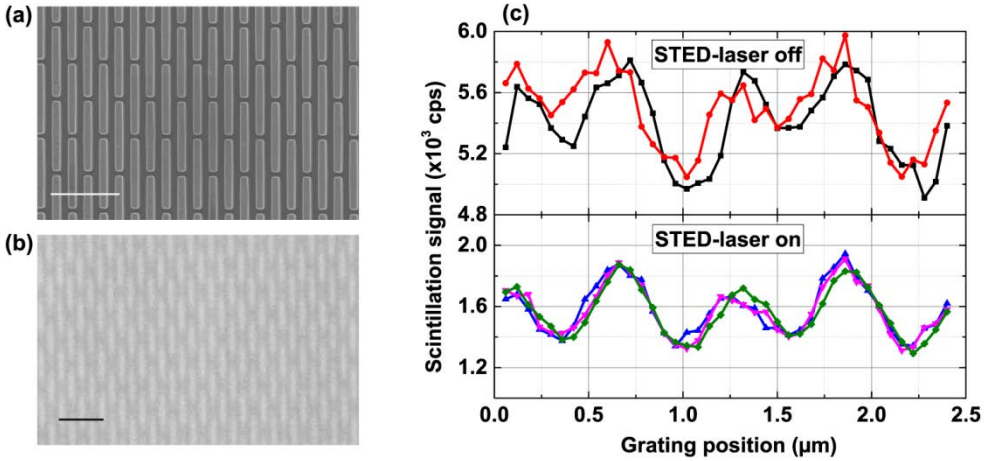

Fig. 8. Images of the 300 lw grating: (a) SEM; (b) dark- and flat-field corrected full-field X-ray image made with a CCD camera with the setup of Fig. 1. Scale bars are 2.5 μm. (c) SSED X-ray imaging scans made along the scale-bar line of Fig. (b) with the STED-laser switched off and on.

For the 300 nm lw grating, the measurements demonstrate an average-visibility improvement from 5% without the STED-laser to 13% with the STED-laser, see Fig. 8(c). The measurements with the 16 μm X-ray pinhole resulted in <2.5% visibilities, as was expected due to the larger fraction of the registered scintillation from outside the confocal volume. According to Eq. (2), a 2-3 fold resolution improvement can be expected for a 100 mW STED-laser applied to LSO:Tb [34]. Our measured visibility improvement is apparently far from optimum, but it clearly demonstrates the feasibility. To quantify the resolution limits of SSED imaging, more measurements with lower aberrations and reduced background due to out-of-confocal volume scintillation are needed.

5. Outlook

X-ray imaging methods based on X-ray optics by now reached sub-100 nm to sub-10 nm resolution. In particular, the use of diffractive zone plates allows <20 nm resolution in the hard X-ray regime [53]. With reflective optics, <10 nm resolution is achievable [54]. With refractive lenses [55], an X-ray beam can be focused to <50 nm [56], and with Laue lenses to 7 nm spot sizes [57] potentially reaching 1 nm [58]. These methods, however, rely on the

Optics EXPRESS

fabrication of X-ray optics. Several of them also require coherent and monochromatic X-ray beams. Furthermore, the imaging can be time-consuming, especially for the case of scanning techniques.

The SSED X-ray imaging method, proposed and demonstrated in this work, offers a solution without the involvement of X-ray optics, and without relying on coherent or monochromatic X-ray sources. To compete with X-ray optics based methods, SSED X-ray imaging needs to have comparable speed and spatial resolution. The latter is fundamentally limited by the spread of the deposited X-ray energy, the effect of which was estimated in this work as <50 nm at 10% contrast for certain hard X-ray energy ranges, see Fig. 4.

Raster scanning a single doughnut beam is too slow for practical applications. For example, a single radiography scan of 10x10 μm^2 area with 100 nm resolution will require 50 nm step sizes, or 40,000 steps in total. With 1 sec pixel dwell time, necessary to accumulate 500-1000 counts per pixel for reasonable SNR, the total scan would last 11 hours. Therefore, for practical applications, a parallelization of SSED X-ray imaging is required, perhaps adopting a solution from super-resolution microscopy [51]. For this, we would require the depletion at $10^2 \ldots 10^3$ fold lower laser powers than what is obtained for Tb^{3+} transitions used in this work. One of the potential candidates is Nd^{3+}. For example, the 1064 nm transition of YVO:Nd has a stimulated emission cross-section of 1.56×10^{-18} cm^2 and a radiative lifetime of 115 μs [59]. Recently demonstrated depletion via up-conversion also requires several-order lower laser power [60]. Charge transfer transition from the valence band to 4f levels of the lanthanides, or even ESA which cross-section can reach 10^{-17} cm^2 in case of YAG:Ce^{3+} [11] can be exploited. Other dense scintillator materials, such as $Bi_4Ge_3O_{12}$ or $CdWO_4$, are interesting candidates.

Besides X-ray imaging, the SSED with its sub-50-nm resolution can potentially find applications in scintillator research. For example, the radiation spread and energy transfer mechanisms could be studied by mapping the scintillator response to a tunable-energy nano-focused X-ray, electron, or proton beams.

6. Summary

We have introduced the concept for stimulated scintillation emission depletion (SSED) X-ray imaging. It is based on the combination of conventional scintillator-based X-ray imaging with STED nanoscopy. Its advantage is potentially superior spatial resolution, which could go beyond the scintillation diffraction barrier (< 300 nm) without the requirement of coherent or monochromatic X-rays and without the use of X-ray optics. This is achieved by confining the scintillator excitation to sub-diffraction sized volumes with a STED-laser, and detecting scintillation from these volumes in a raster-scan mode.

The requirements for the scintillator material, the STED laser, the X-ray energy, and the X-ray flux for SSED X-ray imaging were investigated. The limits of spatial resolution due to finite volume X-ray energy deposition, estimated with GEANT4 Monte Carlo simulations, are far beyond the diffraction barrier. For example, the resolution due to X-ray interaction in LSO is < 50 nm at 10% MTF for 8-15 keV and ~65 keV X-rays. The photodetector signal due to the scintillation emission from the doughnut zero-intensity volume was calculated for LSO:Ce and LSO:Tb scintillators and a conventional microscope using the X-ray absorbed-dose coefficients derived from the MC simulations. A flux of 10^{12} ph/mm^2/s of 10 keV X-rays results in ~800 photodetector cps in case of the Ø 100 nm doughnut center, and ~30 cps in case of the Ø 30 nm one. Due to high flux requirement, the SSED X-ray imaging is rather applicable at synchrotron facilities.

Proof-of-concept experiments, performed with the 1.6 μm think LSO:Tb scintillator and the 628 nm cw STED-laser, demonstrated feasibility of the SSED X-ray imaging. First, X-ray excited scintillation was efficiently depleted with the STED-laser. No additional excitation due to interaction of STED-laser photons with X-ray absorption products was observed. Second, the contrast of the 300 nm line-width grating imaging was improved from 5% to 13%

Optics EXPRESS

by applying SSED. This improvement is apparently far from optimum. The obtained STED-doughnut was distorted by astigmatism as a result of birefringence of the scintillator substrate. Imaging contrast was deteriorated by detection of the scintillation from outside the confocal volume that could not be depleted.

For practical applications, the aberrations and the detection of out-of-confocal-volume scintillation need to be minimized. Furthermore, the parallelization of the SSED is required, first, to compete speed-wise with current X-ray imaging methods based on X-ray optics, and second, to improve the imaging contrast by reducing the detection of the background scintillation.

Funding

Part of this work has been supported by the ERC grant ERC-2012-StG 310005-PhaseX.

Acknowledgments

M. Alekhin thanks Thierry Martin for LSO:Tb; Gordan Mikuljan, Thomas Steigmeier, Iwan Jerjen, and Tine Celcer for technical assistance; Achint Jain, Rene Reimann, Vijay Jain, and Mark Kasperczyk for sharing optical expertise; Christian Schlepütz, Joan Vila Comamala, Pablo Villanueva, and Matias Kagias for sharing beam-line expertise; Konstantins Jefimovs and Christian David for suggestions on X-ray pinholes and X-ray absorption gratings; and Andrey Vasil'ev and Richard Williams for discussions on scintillator energy transport mechanisms.